Measuring device for synchrotron X-ray imaging and first results of high temperature polymer electrolyte membrane fuel cells

R. Kuhn[a], J. Scholta[a,*], Ph. Krüger[a], Ch. Hartnig[a,1], W. Lehnert[b], T. Arlt[c], I. Manke[c]

[a] *Zentrum für Sonnenenergie- und Wasserstoff-Forschung Baden-Württemberg (ZSW), Helmholtzstr. 8, 89081 Ulm, Germany*
[b] *Institute of Energy Research – Fuel Cells (IEF-3), Forschungszentrum Jülich GmbH, 52425 Jülich, Germany*
[c] *Helmholtz Center Berlin for Materials and Energy (HZB), Glienicker Straße 100, 14109 Berlin, Germany*

ABSTRACT

In this paper, a measurement cell for recording synchrotron X-ray images of low and high temperature PEM fuel cells is described. The experimental setup allows for recording of cross-sectional images, as well as for radiograms in through-plane direction, with limited signal degradation. First results on H_3PO_4 concentration and distribution as a function of the operating conditions are presented.

This basic cell design is optimized for liquid water detection. To visualize water in an operating cell the energy of the synchrotron X-ray beam has been chosen in a range between 7 and 30 keV where high resolution images can be obtained. The cell design is described in detail, and references to results obtained with LT-PEMFC applications focusing on liquid water evolution are given. For HT-PEMFC applications, the method of synchrotron X-ray imaging can provide an insight on electrolyte concentration and distribution. These investigations show that significant information can be collected on electrolyte distribution and concentration as a function of operating parameters such as temperature, media utilization and humidification degree. First results for the dependence of electrolyte distribution on operating conditions are presented.

1. Introduction

Previously, many investigations on the water inventory of low temperature PEMFC have been conducted, employing non-destructive methods such as neutron or synchrotron X-ray imaging [1–17]. In high temperature fuel cells, adequate studies analyzing the water inventory which directly corresponds to concentration and distribution changes of H_3PO_4 have not been approached. To further elucidate these processes a special measurement setup has been developed: the cell has been successfully used for recording synchrotron images of low and high temperature PEM fuel cells. The measurement cell allows for collection of through plane images as well as for radiograms of the in-plane direction with very small signal weakening. Additionally, the measurement cell has an active area of appr. 60 cm^2 which allows the cell to be operated with utilization degrees typical for realistic fuel cells excluding most of possible artifacts by design.

In this paper, the cell design is described in detail and first results on H_3PO_4 concentration and distribution dependent on the operating conditions are given. References to results obtained with this cell in the field of LT-PEMFC applications are also given. In low temperature applications the water inventory of all active components, especially of the GDL and the flowfield channels, plays an important role in the design of a high performing fuel cell.

For HT-PEMFC, traditional water inventory is not relevant since all water should be present in the gaseous phase at typical operating temperatures of 160 °C such that no water droplets or diffusion barriers can occur [18,19]. Nonetheless, the method of synchrotron X-ray imaging can provide an insight on electrolyte concentration and distribution for HT-PEMFC applications. The reason is that depending on the operating parameters changes occur in the concentration of the H_3PO_4 electrolyte. These differences result in modifications of the mass attenuation as function of operating parameters like utilization degrees, humidification and temperature levels. At low operating temperatures, droplets might occur due to the hygroscopic behavior of H_3PO_4 and the resulting dilution of H_3PO_4 which might cause an electrolyte leaching or an enhanced removal of acid from the electrochemically active spots.

The performed investigations show that significant information on the break-in procedure as well as on the electrolyte distribution and concentration as a function of cell operating parameters could be collected. A direct correlation of beam attenuation (signal intensity) and HT-PEMFC operating conditions has been found and is described in detail. Results regarding dimensional changes of fuel cell components are reported in a separate paper [20].

---

* Corresponding author. Tel.: +49 731 9530 206; fax: +49 731 9530 206.
E-mail address: joachim.scholta@zsw-bw.de (J. Scholta).
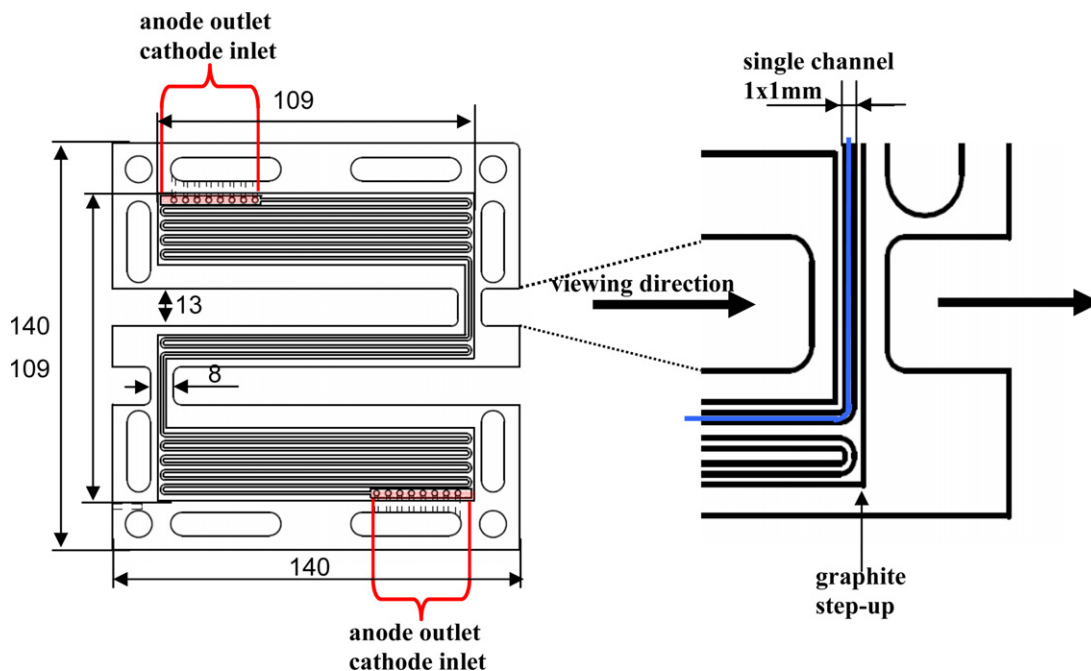[1] Present address: Chemetall GmbH, Frankfurt, Germany.

Fig. 1. Schematic view of the cell optimized for synchrotron studies.

2. Experimental procedure

2.1. Fuel cell design

The measurement cell is specifically designed to allow for recording of cross-sectional images as well as for radiograms in the through-plane direction with very small signal weakening. Water sensitivity and high spatial resolution are achieved by the combined strategy of reducing the material thickness of the cell in the radiographed areas and optimization of the synchrotron beam. The detailed cell design is shown in Fig. 1.

For these investigations (LT-PEMFC, DMFC, HT-PEMFC), the design was based on a modified 100 cm^2 fuel cell. Specifically, changes include reduction of the active area to 60 cm^2 keeping in mind to achieve an improved gas tightness of the cell. With this cell setup, the beam is required to pass in sum only 6.4 mm of graphite resulting in a sufficiently high contrast ratio for the visualisation of small water and electrolyte concentration changes in the fuel cell.

2.2. Fundamentals and test environment

The radiographic measurements were performed with the tomography capabilities of the BAMline at the electron storage ring BESSY II. A monochromatic X-ray beam with energies in the range between 6 and 80 keV is available. Provided with the optimized energy, the monochromatic beam allows for an optimal quantification of the liquid water distribution in a DMFC or a LT-PEMFC; beam hardening artifacts caused by the energy dependent attenuation coefficient are avoided. The difference of compound specific mass attenuation coefficients leads to different grey values in the images. The collected radiographs of operating fuel cells and their water content were normalized with reference to the same assembly in the dry condition; in high temperature applications a 'dry' condition means a cell setup without any external potential applied so that the electrochemical (water producing reaction) can be stopped and no electrolyte dilution has been observed. Dividing the two grey scale radiographies led to an image that shows only the change in the fuel cell caused by the water content. The transmission through the cell is given by the Beer-Lambert law,

$$I = I_0 e^{- \int \mu(x) dx} \tag{1}$$

where I_0 is the primary beam intensity, I the detected beam intensity, x the propagation direction, and μ the attenuation coefficient. As shown in (1), the amount of the transmitted synchrotron beam is dependent on the integral attenuation coefficient in beam direction. Regarding the fuel cell design for synchrotron investigation, the cell size in the beam direction should be constructed to be as small as possible considering electrical and mechanical boundary conditions. Metals and other high absorbing materials should be avoided.

In previous studies the visualization method was already successfully applied for investigations on LT-PEMFC [1–3] and DMFC [4], using both in-plane and through-plane views. In LT-PEMFC-experiments, water estimations in the GDL in the flowfield channels were performed, whereas in the DMFC experiments, the dynamics of carbon dioxide bubble formation were observed. In those experiments, the X-ray beam energy has been optimized for water detection. At an energy range between 7 keV and 16 keV the X-ray radiation is highly sensitive to liquid water. In Fig. 2 the dependence of the attenuation coefficients on the beam energy and in Fig. 3 the resulting beam transmission change for H_2O and H_3PO_4 dependent on the total agglomeration thickness in beam direction are shown.

Below 7 keV the X-ray beam is almost totally absorbed by thicker water (or electrolyte) clusters (hardly any transmission and thus no image contrast). At energy levels above 16 keV the transmission rates for most water thicknesses are very high and the sensitivity towards the detection of small water agglomerations is lost. Energy levels of up to 30 keV may be used for HT-PEMFC applications, since the absorption coefficient of H_3PO_4 is approximately a factor of 7 higher than the corresponding value for water. Therefore, a beam energy of 30 keV was selected as a good compromise between signal intensity and selectivity to H_3PO_4.

In Fig. 4, the dependence of the synchrotron transmission on different cases for H_3PO_4 dilution is given.

The accurate interpretation of the graphs should include the total liquid volume and related volume changes as well as H_3PO_4
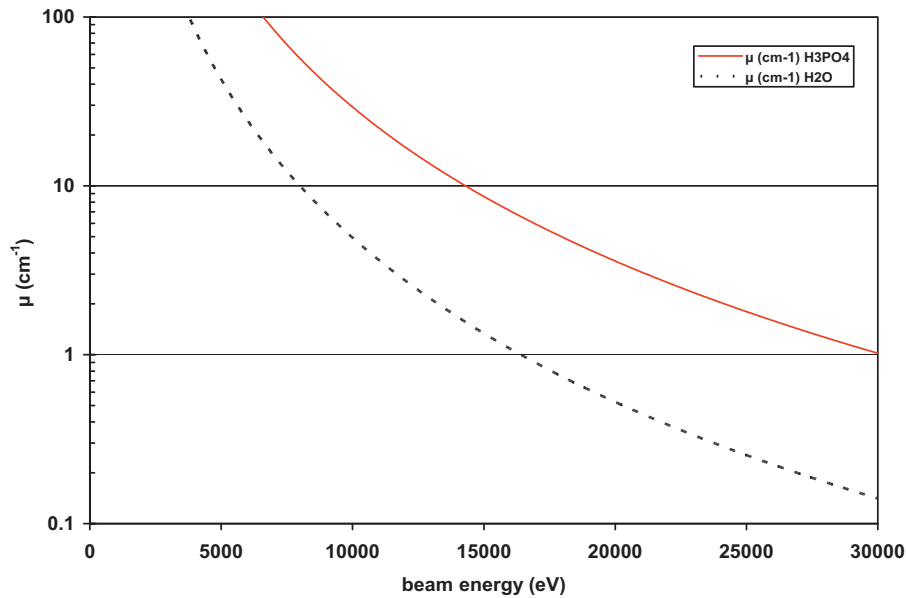
Fig. 2. Synchrotron attenuation coefficient of 100% H_3PO_4 and of water as a function of beam energy.
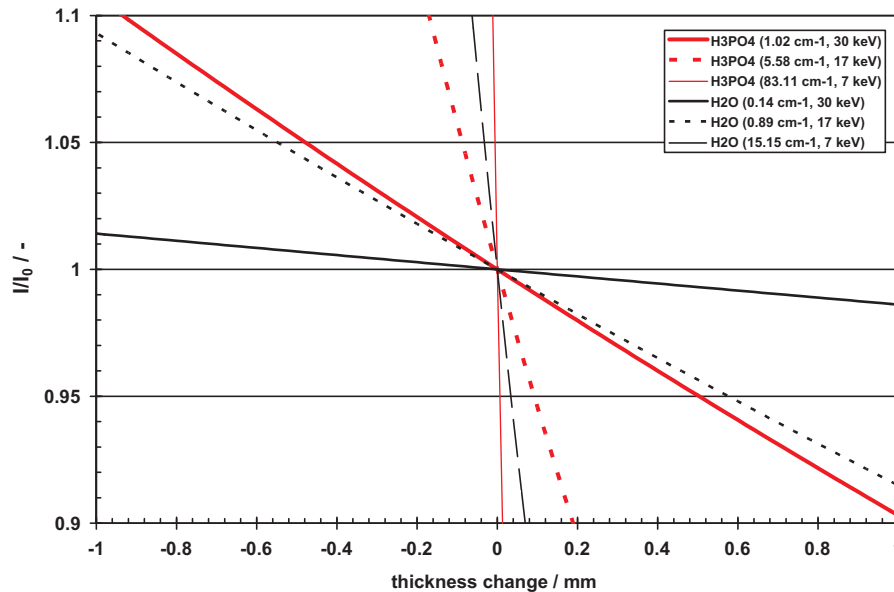

Fig. 3. Synchrotron transmission change as a function of water thickness in the stack assembly, for different beam energies and corresponding attenuation coefficients.

concentration changes. Two factors do influence the overall attenuation factor: in the case of H_3PO_4 dilution a volume increase caused by H_2O occurs, resulting in a significant transmission decrease if the volume increase is combined with a corresponding increase of H_3PO_4 agglomeration thickness in beam direction caused e.g. by an increased pore filling degree in beam direction ("expansion in beam direction"). A different situation holds for the membrane: there H_3PO_4 dilution leads to an expansion preferably in non-beam direction and therefore to a transmission increase due to partial replacement of H_3PO_4 by H_2O. The transmission increase is expected between the cases described by "expansion except beam direction" and "expansion in all directions". In these cases, H_3PO_4 dilution results in a high to moderate transmission increase. For the other areas, it is assumed that gas pores exist, which are partially filled with electrolyte in case of dilution of H_3PO_4 ("expansion in all directions"). In Fig. 5, the transmission change is given for the latter, most relevant cases and different H_3PO_4 reference concentrations.

The H_3PO_4 concentration itself is strongly dependent on the temperature and the water partial pressure in gaseous media. The dependences (derived from equations given in [21]) are shown in Fig. 6.

For visualization of the dynamic behavior in HT-PEMFC with a size of up to $10.0\,mm \times 6.9\,mm$, an optical setup was used that provides $2.5\,\mu m$ pixel size. The temporal resolution was around 5 s, composed of 1 s for exposure time and 4 s for read out of the camera data.

The operation conditions given in Table 1 were analyzed with respect to the water partial pressures resulting both from humidification (anode) and from product water (cathode). Anode water partial pressures were calculated using the Magnus formulae [22]. Cathode water partial pressures were calculated from mass balances. Values were taken at the anode inlet and cathode outlet, and the averaged values were used for the calculation of the expected H_3PO_4 concentration. For the calculations, relationships shown in
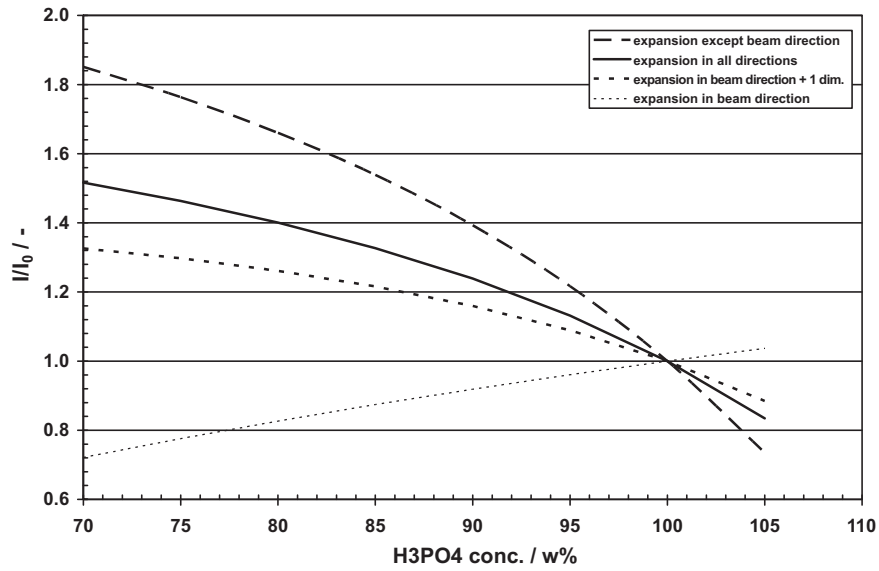
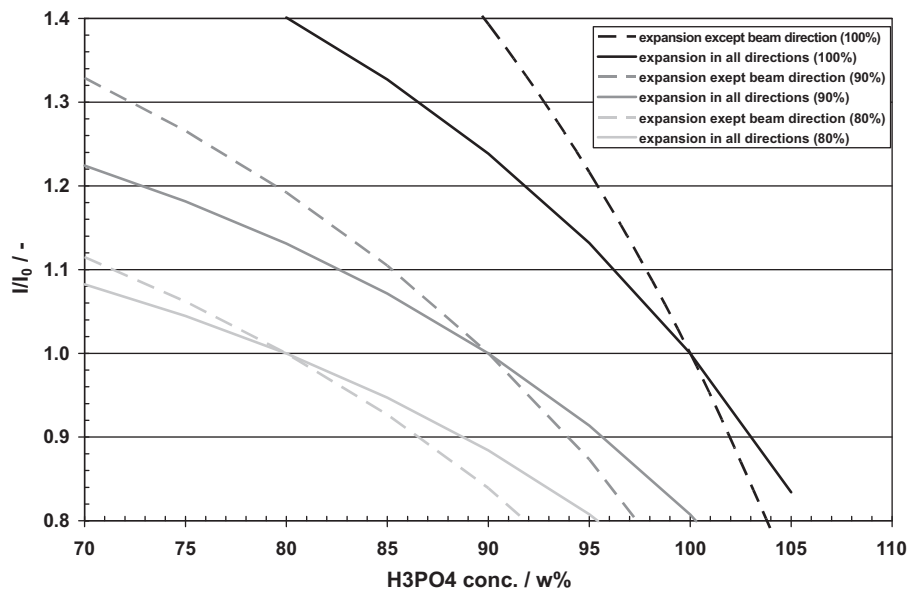**Fig. 4.** Synchrotron transmission change by varying the H_3PO_4 concentration, referring to 100% H_3PO_4.

Fig. 5. Synchrotron signal transmission change by varying the H_3PO_4 concentration, referring to 80, 90, and 100% H_3PO_4.
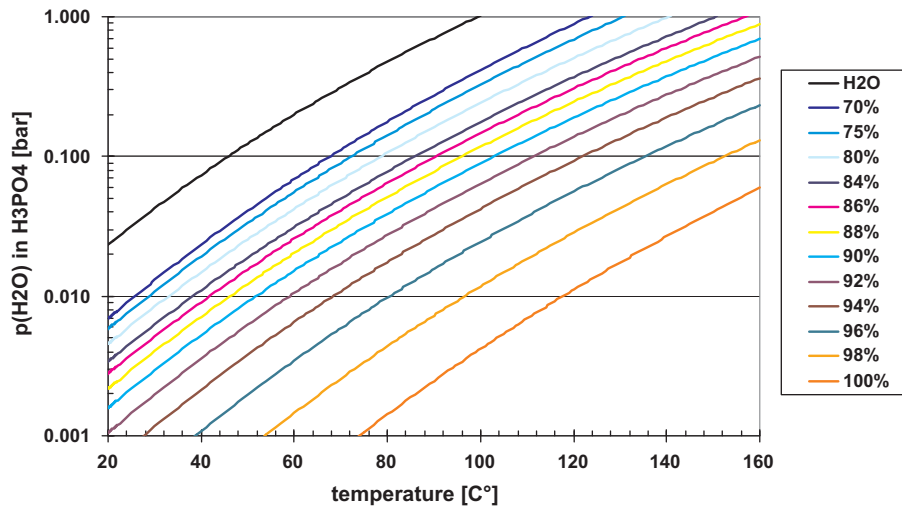

Fig. 6. Water vapour pressure dependent on temperature and H_3PO_4 concentration.

Table 1
HT-PEMFC operating conditions.

| Run and picture no.	Tcell (°C)	Current (A)	Anode flow rate (Nml/min)	Cathode flow rate (Nml/min)	Utilization anode (−)	Utilization cathode (−)	Anode inlet dew point (°C)	Vapour partial pressure anode (mbar)	Vapour partial pressure cathode (mbar)	av. vapour pressure (mbar)	Weight % H_3PO_4
I											
1	149	0.0	80	200	0.000	0.000	0	6.0	0.0	3.0	103.6
2	149	11.2	87	213	0.895	0.883	0	6.0	243.7	124.9	97.0
3	149	0.0	480	1200	0.000	0.000	0	6.0	0.0	3.0	103.6
4	149	11.2	480	1200	0.162	0.157	0	6.0	49.2	27.6	00.6
IV											
5	152	11.2	87	213	0.895	0.883	70	310.6	243.7	277.2	94.0
6,7	152	0.8	80	200	0.070	0.067	70	310.6	21.4	166.0	96.2
8	151	11.2	87	533	0.895	0.353	70	310.6	107.2	208.9	95.3
9	152	0.8	80	200	0.070	0.067	70	310.6	21.4	166.0	96.2
10,11	151	11.2	87	2140	0.895	0.088	70	310.6	27.9	169.3	96.1
12	151	0.8	80	200	0.070	0.067	70	310.6	21.4	166.0	96.2
13,14,15	152	11.2	87	213	0.895	0.883	0	6.0	243.7	124.9	97.3
16,17,18	152	0.8	80	200	0.070	0.067	0	6.0	21.4	13.7	102.0
19	152	11.2	87	533	0.895	0.353	0	6.0	107.2	56.6	99.4
20,21	153	0.8	80	200	0.070	0.067	0	6.0	21.4	13.7	102.0
22,23	152	11.2	87	2140	0.895	0.088	0	6.0	27.9	17.0	101.7
24	152	0.8	80	200	0.070	0.067	0	6.0	21.4	13.7	102.0
V											
Seq.1	75	4.0	80	200	0.348	0.336	70	310.6	102.3	206.5	57.3
Seq.2	75	0.8	80	200	0.070	0.067	70	310.6	21.4	166.0	65.1
VI,19 kev											
25	75	0.8	80	200	0.070	0.067	70	310.6	21.4	166.0	64.8
26	75	4.0	80	200	0.348	0.336	70	310.6	102.3	206.5	57.4
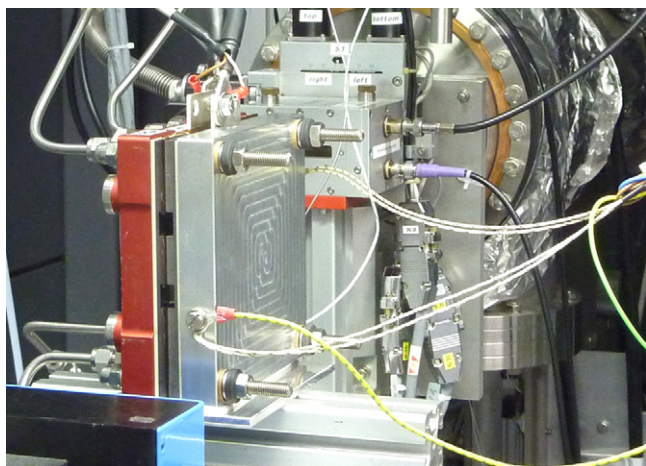
Fig. 7. Location of the HT-PEMFC in the radiography setup, shown in viewing direction from the camera.

Fig. 6 were used. It was assumed for the calculations that no water transfer occurs between the anode and the cathode. Dew points of unhumidified media were assumed to be 0 °C. The resulting H_3PO_4 concentrations are also given in Table 1. The described assumptions are simple, but allow a good prediction of the local concentrations in this stage. A more elaborate model may be used, if the relevant diffusion parameters of the used MEA are known in full detail.

3. First HT-PEMFC measurements

3.1. Set up of HT-PEMFC test cell

The design of the HT-PEMFC cell is shown in Fig. 1. Modifications were mainly done with respect to sealing (higher resistance to thermal and chemical stress, limitation of compression set). The detailed experimental layout of the cell in the test bench is shown in Fig. 7.

The cell design is modified such that after assembly a defined compressed thickness of the MEA is adjusted. The MEA used for this test has been manufactured by FZJ. Details about MEA preparation, cell assembly and start up procedures can be found elsewhere [23–25].

3.2. Test plan

The testing parameters were designed to give significant information on the electrolyte distribution and concentration as a function of the operating parameters like temperature, media utilization and humidification degree. In this article, all concentra-

tions are given relative to H_3PO_4, which represents the mixture of ortho-phosphoric acid (H_3PO_4) and pyrophosphoric acid ($H_4P_2O_7$) occurring at concentrations close to 100% H_3PO_4. A data set of operating conditions is given in Table 1.

4. Results

For HT-PEMFC, the water inventory in a conventional way is not relevant as all water should be present in the gaseous stage; this in turn means that no water droplets or diffusion barriers can occur in normal operating conditions. Nonetheless, the method of synchrotron X-ray imaging provides an insight on electrolyte concentration and distribution for HT-PEMFC applications. The reason is that concentration and therefore mass attenuation changes of H_3PO_4 electrolyte occurs depending on operating parameters.

In general, the measurement of a large fuel cell at temperatures around 150 °C is very challenging since small thermal creeps resulting in mechanical shifts in the μm scale may occur after every change of the operating parameters, especially of the temperature. However the cell movement could be mostly corrected by special software tools. The performed variations (given in Table 1) show significant changes in synchrotron X-ray images. All images and diagrams show the anode on the right and the cathode on the left side. From left to right are displayed: cathode GDL, cathode electrode, membrane, anode electrode, anode GDL (see Fig. 8a). In the following part, the influence of the current density (c.d.) and the air utilization on the fuel cell performance are described and discussed in more detail:

4.1. Influence of current density on electrolyte concentration

In Fig. 8, two intensity ratio images on high/low current flow of a HT-PEMFC are given.

It is observed that the water production at higher cell temperatures (av. temp of 150 °C) leads to significant absorption changes (higher transmission) in the membrane once an external load is applied both for high and low air utilization ratios. Since the void volume in the gas diffusion media which is accessible for liquids is filled and thus constant for both cases, increases in transmission must correspond to a lower H_3PO_4 concentration. This is in agreement with the higher water vapour content at the cathode side under operation conditions. As expected from H_3PO_4 concentration data in Table 1, the change in concentration is smaller for low air utilization (c) than for high air utilization (b). An estimation using the I/I_0 data derived from Fig. 5, shows that in the membrane area H_3PO_4 concentration changes between 1.5 and 3% can be observed which is slightly lower than expected from Table 1 but is in general in agreement with the expected behavior.

In the GDL areas, hardly any significant transmission changes have been observed leading to the conclusion that only small H_3PO_4
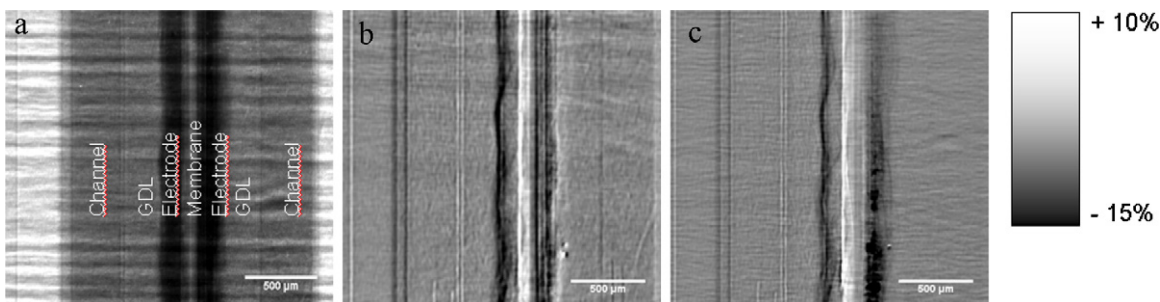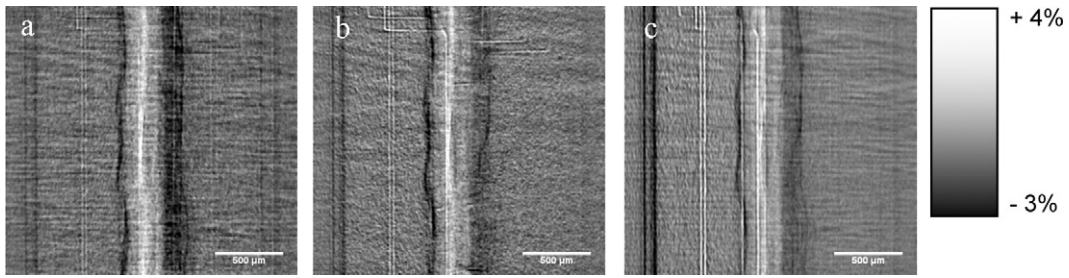

Fig. 8. (a) Location of channels, GDL, electrodes and membrane for Figs. 7–13 and (b) current density ratio picture (11.2 A/0.8 A), picture (p.) 2 div p. 1, (b) p. 4 div p. 3, operating conditions: 11.2 A, $dp_{anode} = 0$ °C, $T_{cell,av.} = 149$ °C, anode flow = 87 ml min^{-1}, cathode flow (b) = 213 ml min^{-1} (90%), cathode flow (c) = 1200 ml min^{-1} (16%), scale on right side: intensity ratio deviation from 1.00 in%.

Fig. 9. Current density ratio picture (11.2 A/0.8 A) (a) p. 13 div p. 17, (b) p. 19 div p. 21, (c) p. 23 div p. 24, operating conditions: 11.2 A, $dp_{anode} = 0\,°C$, $T_{cell,av.} = 152\,°C$, anode flow = 87 ml min^{-1}, cathode flow (a) = 213 ml min^{-1} (90%), cathode flow (b) = 533 ml min^{-1} (35%), cathode flow (c) = 2140 ml min^{-1} (9%).
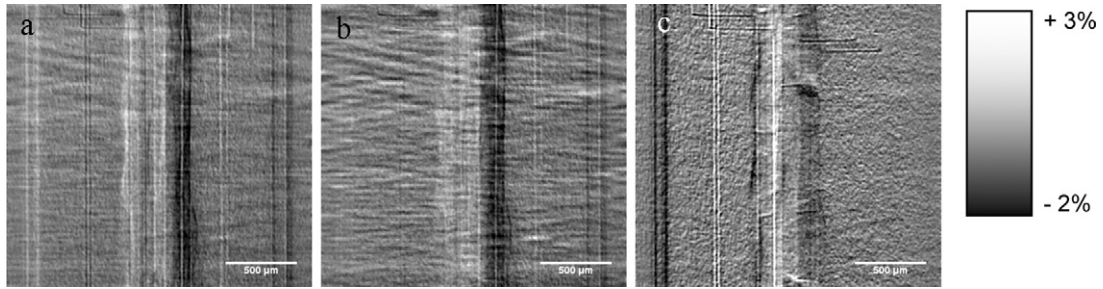
Fig. 10. (a) Current density ratio picture (11.2 A/0.8 A), p. 5 div p. 6, (b) p. 8 div p. 9, (c) p. 11 div p. 12, operating conditions: 11.2 A, $dp_{anode} = 70\,°C$, $T_{cell,av.} = 150\,°C$, anode flow = 87 ml min^{-1}, cathode flow (a) = 213 ml min^{-1} (90%), cathode flow (b) = 533 ml min^{-1} (35%), cathode flow (c) = 2140 ml min^{-1} (9%).
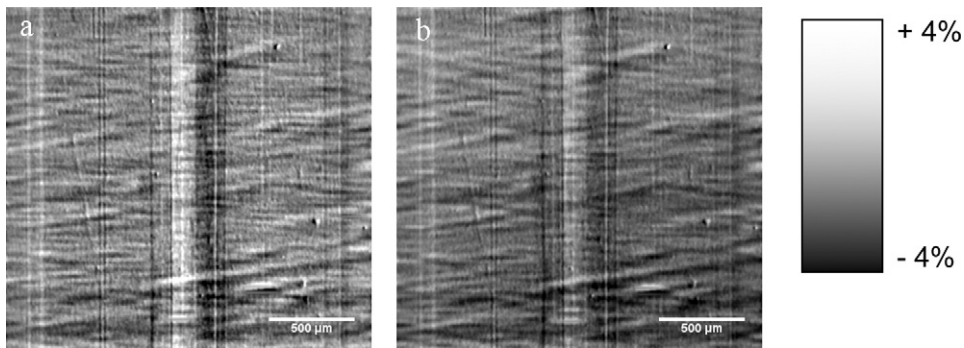
**Fig. 11.** Dew point ratio pictures, $dp_{anode} = 70\,°C/dp_{anode} = 0\,°C$ (a) p. 10 div p. 22, (b) p. 7 div p. 16, operating conditions: anode flow = 87 ml min^{-1}, $T_{cell,av.} = 150\,°C$, (a) 11.2 A, 9% air utilization, (b) 0.8 A, 200 ml min^{-1} air flow.

amounts are located in the GDL where concentration and/or volume changes do not have a significant effect.

In the electrodes, only small absorption increase can be observed at the cathode while on the anode side a higher change has been observed. In these areas a possible change in the liquid volume must be considered. Since the H_3PO_4 concentration at the cathode electrode cannot be higher under external load than under OCV conditions, the observed darkening must correspond to an increase in H_3PO_4 volume, which in turn indicates a higher level of pore filling. At the anode, a stronger darkening under current flow was observed corresponding to a H_3PO_4 volume and/or concentration increase.

A second series of current density ratio pictures is given in Figs. 9 and 10. In both cases, a higher transmission in the membrane
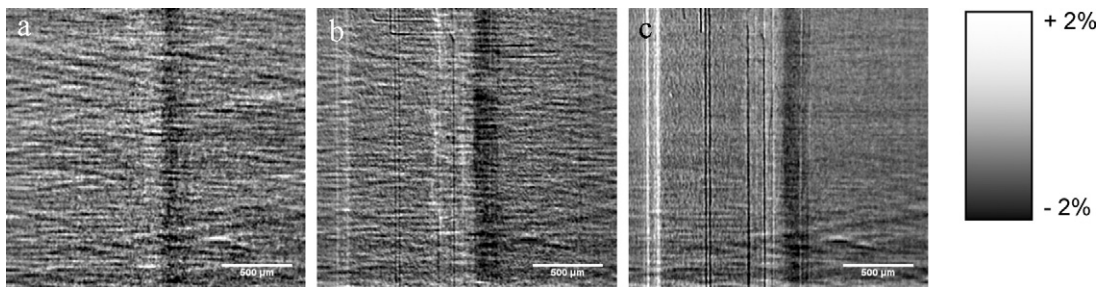
Fig. 12. (a) Utilization ratio picture, p. 18 div p. 20, (b) p. 14 div p. 19, (c) p. 15 div p. 23, operating conditions: 11.2 A, $dp_{anode} = 0\,°C$, anode flow = 87 ml min^{-1}, $T_{cell,av.} = 153\,°C$, (a) 0.8 A/0.8 A anode flow = 80 ml min^{-1}, cathode flow = 200 ml min^{-1} (no parameter change, reproducibility test), (b) air utilization ratio 90%/35%, (c) air utilization ratio 88%/9%.
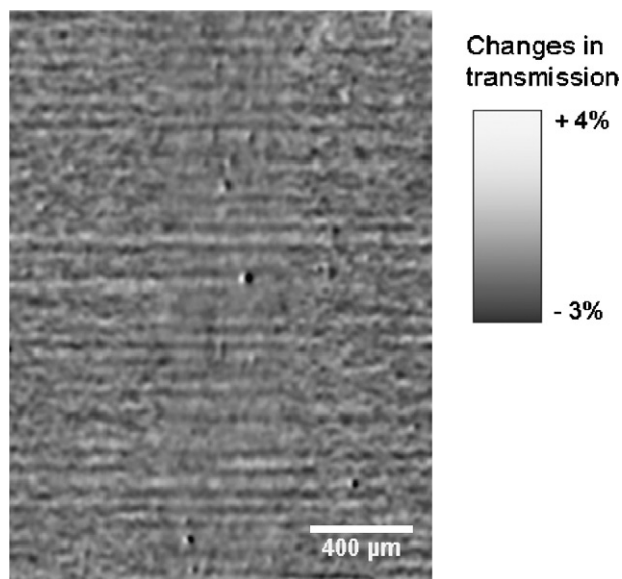
Fig. 13. Current density ratio picture (4 A, air utilization 35%)/0.8 (A), p. 26 div p. 25, operating conditions: $T_{cell,av.} = 75\,°C$, $dp_{anode} = 70\,°C$, anode flow = 80 ml min^{-1}.

area (appr. 1–3%) can be observed, indicating a H$_3$PO$_4$ dilution of appr. 1% when current is applied. On the other hand, a transmission decrease in the anode area can be observed. This transmission decrease is enhanced at high cathode utilization rates. The behavior can be explained mainly by a H$_3$PO$_4$ concentration increase, maintaining a comparable pore filling degree. The described behavior is present both for unhumidified (Fig. 9) and humidified (Fig. 10) cathode gas flows, however, transmission changes are slightly smaller in case of the humidified cathode gas.

The influence of humidification on H$_3$PO$_4$ concentration is shown in Fig. 11.

In the membrane area, the transmission increases which can be converted to an estimated H$_3$PO$_4$ dilution of slightly above 0.5% as the influence of increasing current. In the electrode area of both anode and cathode, a small transmission decay can be observed. Since the H$_3$PO$_4$ concentration is expected to decrease not only in the membrane, the slight darkening is expected to correspond with a slight increase in total liquid volume as well as in the degree of liquid pore filling.

4.2. Influence of air utilization on electrolyte concentration and distribution

In Fig. 12, two consecutive images of the HT-PEM cell operated on high/low air utilization is shown. Fig. 12(a) indicates that after a settlement time of 5 min (ratio picture after 7.5 min and 5 min settlement time) under close to OCV conditions almost no transmission changes can be observed, indicating a stable cell status. Fig. 12(b) and (c) indicate that an utilization increase also leads to a significant H$_3$PO$_4$ dilution (≤0.5%, as observed in the membrane area). At the cathodic electrode, no clear tendency can be observed, whereas at the anode, a certain increase in pore filling degree (transmission decay) is shown.

4.3. Influence of temperature changes on electrolyte distribution

Summarizing the results at cell temperatures of around 150 °C, the water resulting from faradayic processes leads to significant but not tremendously high changes in the electrolyte distribution: in the membrane area, a certain H$_3$PO$_4$ dilution occurs, whereas in the electrode areas small concentration changes and/or volume changes can be observed.

The situation changes significantly if the operating temperature is decreased down towards 70 °C, and a media humidification is applied. In that case, the H$_3$PO$_4$ concentration is mainly influenced by the external humidification and only to a very small extent by
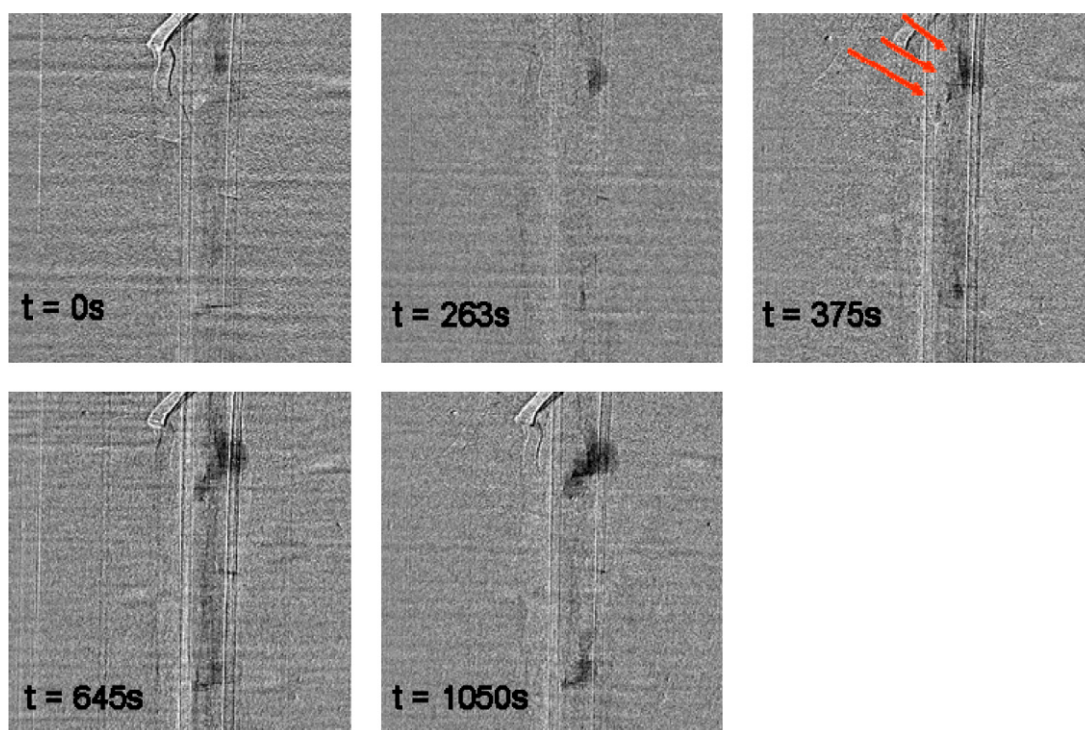
Fig. 14. p. Seq. 1, Seq. 2 (Seq. 1: 1, 2, 3, Seq.2: 4, 5) operating conditions: p. Seq. 1: 4 A, p. Seq. 2: 0.8 A, $T_{cell,av.} = 75\,°C$, $dp_{anode} = 70\,°C$, anode flow = 80 ml min^{-1}, cathode flow 200 ml min^{-1}.

the product water. This thesis has been proven by the normalizing images taken at "external current (4 A)" and "no external current" with respect to each other (Fig. 13), where almost no transmission change in any region has been observed; the product water stemming from the electrochemical processes has almost no influence on the H_3PO_4 concentration if superimposed by the influence of the external humidification.

In addition, for low operating temperatures, a droplet formation of diluted H_3PO_4 has been observed. Fig. 14 shows such a formation of a droplet at the anode side.

The droplet formation on the anode side is caused by H_3PO_4 dilution and also continues in the low current phase (0.8 A) of the test cycle. It will be an interesting topic for further research to find out the boundary conditions for droplet free operating parameters.

5. Summary

The performed investigations show that synchrotron X-ray imaging with an adapted cell design can be used to study the electrolyte in an operating HT-PEMFC. Significant information on the electrolyte distribution and concentration as a function of the operating parameters like temperature, media utilization and humidification degree have been collected. Moreover, boundary conditions for droplet formation free operating conditions can be identified which serve as basis for operating strategies to prevent electrolyte leaching to a large extent.

References

[1] Ch. Hartnig, I. Manke, R. Kuhn, N. Kardjilov, J. Banhart, W. Lehnert, Appl. Phys. Lett. 90 (2008) 134106.
[2] I. Manke, C. Hartnig, H. Riesemeier, J. Goebbels, N. Kardjilov, R. Kuhn, P. Krüger, J. Banhart, Fuel Cells 10 (1) (2010) 26–34.
[3] I. Manke, Ch. Hartnig, M. Grünerbel, W. Lehnert, N. Kardjilov, A. Haibel, A. Hilger, H. Riesemeier, J. Banhart, Appl. Phys. Lett. 90 (2007) 174105.
[4] Ch. Hartnig, I. Manke, J. Schloesser, Ph. Krüger, R. Kuhn, H. Riesemeier, K. Wippermann, J. Banhart, Electrochem. Commun. 11 (2009) 1559–1562.
[5] Ch. Hartnig, I. Manke, N. Kardjilov, A. Hilger, M. Grünerbel, J. Kaczerowski, J. Banhart, W. Lehnert, J. Power Sources 176 (2008) 452–459.
[6] Ch. Hartnig, I. Manke, R. Kuhn, S. Kleinau, J. Goebbels, J. Banhart, J. Power Sources 188 (2009) 468–474.
[7] Ch. Hartnig, R. Kuhn, Ph. Krüger, J. Schloesser, I. Manke, Proceeding, FDFC-2008, Nancy, online avail able (2009).
[8] Ch. Hartnig, R. Kuhn, Ph. Krüger, I. Manke, N. Kardjilov, J. Goebbels, B.R. Müller, H. Riesemeier, MP Mater. Test. – Mater. Compon. Technol. Appl. 50 (2008) 609–614.
[9] I. Manke, N. Kardjilov, A. Haibel, C. Hartnig, M. Strobl, A. Rack, A. Hilger, J. Scholta, W. Lehnert, W. Treimer, S. Zabler, J. Banhart, DGZfP-Berichtsband 94 (2005) 60, ISBN 3-931381-64-1.
[10] R. Thiedmann, Ch. Hartnig, I. Manke, V. Schmidt, W. Lehnert, J. Electrochem. Soc. 156 (11) (2009) B1339–B1347.
[11] R.J. Bellows, M.Y. Lin, M. Arif, A.K. Thompson, D. Jacobson, J. Electrochem. Soc. 146 (1999) 1099–1103.
[12] R. Satija, D.L. Jacobson, M. Arif, S.A. Werner, J. Power Sources 129 (2004) 238–245.
[13] L. Carrette, K.A. Friedrich, U. Stimming, Fuel Cells 1 (1) (2001) 5–39.
[14] D. Kramer, E. Lehmann, G. Frei, P. Vontobel, A. Wokaun, G.G. Scherer, Nucl. Instrum. Methods Phys. Res. A 542 (2005) 52–60.
[15] K.W. Feindel, S.H. Bergens, R.W. Wasylishen, J. Power Sources 173 (2007) 86.
[16] J.J. Kowal, A. Turhan, K. Heller, J. Brenizer, M.M. Mench, J. Electrochem. Soc. 135 (2006) A1971–A1978.
[17] A. Turhan, K. Heller, J.S. Brenizer, M.M. Mench, J. Power Sources 180 (2008) 773–783.
[18] J. Scholta, R. Kuhn, S. Wazlawik, L. Jörissen, ECS Trans. 17 (1) (2009) 325.
[19] J. Scholta, M. Messerschmidt, L. Jörissen, Ch. Hartnig, J. Power Sources 190 (2009) 83–85.
[20] W. Maier, T. Arlt, Ch. Wannek, I. Manke, H. Riesemeier, Ph. Krüger, J. Scholta, W. Lehnert, J. Banhart, D. Stolten, Electrochem. Commun. 12 (10) (2010) 1436–1438.
[21] D.I. MacDonald, J.R. Boyack, J. Chem. Eng. Data 14 (1969) 380–384.
[22] O. Tetens, Z. Geophys. 6 (1930) 297–309.
[23] C. Wannek, B. Kohnen, H.F. Oetien, H. Lippert, J. Mergel, Fuel Cells 8 (2008) 87.
[24] C. Wannek, W. Lehnert, J. Mergel, J. Power Sources 192 (2009) 258–266.
[25] C. Wannek, I. Konradi, J. Mergel, W. Lehnert, Int. J. Hydrogen Energy 23 (2009) 9479.